The Astrophysical Journal, 971:136 (15pp), 2024 August 20 https://doi.org/10.3847/1538-4357/ad5674

A Spectral Atlas of Lyα Emitters at $z = 5.7$ and $z = 6.6$

A. Songaila[1], L. L. Cowie[1], A. J. Barger[1,2,3], E. M. Hu[1], and A. J. Taylor[2,4]
[1] Institute for Astronomy, University of Hawaii, 2680 Woodlawn Drive, Honolulu, HI 96822, USA; acowie@ifa.hawaii.edu
[2] Department of Astronomy, University of Wisconsin-Madison, 475 N. Charter Street, Madison, WI 53706, USA
[3] Department of Physics and Astronomy, University of Hawaii, 2505 Correa Road, Honolulu, HI 96822, USA
[4] Department of Astronomy, The University of Texas at Austin, 2515 Speedway, Austin, TX 78712, USA
Received 2024 February 12; revised 2024 May 13; accepted 2024 May 28; published 2024 August 13

Abstract

We present two uniformly observed spectroscopic samples of Lyα emitters (LAEs; 127 at $z = 5.7$ and 82 at $z = 6.6$), which we use to investigate the evolution of the LAE population at these redshifts. The observations cover a large field (44 deg^2) in the North Ecliptic Pole, as well as several smaller fields. We have a small number of exotic LAEs in the samples: double-peaked Lyα profiles; very extended red wings; and one impressive lensed LAE cross. We also find three broad-line active galactic nuclei. We compare the Lyα line width measurements at the two redshifts, finding that the lower-luminosity LAEs show a strong evolution of decreasing line width with increasing redshift, while the high-luminosity LAEs do not, with a transition luminosity of log $L(\mathrm{Ly}\alpha) \approx 43.25$ erg s^{-1}. Thus, at $z = 6.6$, the high-luminosity LAEs may be producing large ionized bubbles themselves, or they may be residing in overdense galaxy sites that are producing such bubbles. In order to avoid losses in the red wing, the radius of the ionized bubble must be larger than 1 pMpc. The double-peaked LAEs also require transmission on the blue side. For the four at $z = 6.6$, we use models to estimate the proximity radii, R_a, where the ionizing flux of the galaxy is sufficient to make the surroundings have a low enough neutral fraction to pass the blue light. Since the required R_a are large, multiple ionizing sources in the vicinity may be needed.

Unified Astronomy Thesaurus concepts: Cosmological evolution (336); Lyman-alpha galaxies (978); Reionization (1383)

Materials only available in the online version of record: FITS file

1. Introduction

The epoch of reionization is a key time in the evolution of the Universe, when the intergalactic medium (IGM) transitioned from being neutral to being very highly ionized. As we discuss below, it is likely that reionization is patchy and that the ionization begins with HII regions around the ionizing sources, which then expand and merge. However, our understanding is still quite limited. Intensive simulations are currently being carried out to model this evolution, but there are many issues that can only be treated in an empirical fashion. Perhaps most critically, we still do not know which objects were the source of the photons that reionized the IGM, nor the exact redshift range when reionization occurred. Answering these questions is a major goal of observational cosmology and fundamental for simulating galaxy evolution.

There has been enormous recent progress in identifying populations of high-redshift galaxies, in particular Lyα emitters (LAEs) at $z \gtrsim 6$. These samples have the potential to constrain when reionization occurred, since both the strength and shape of the Lyα line can be modified by the radiative damping wings of neutral hydrogen in the IGM (e.g., Haiman 2002; Haiman & Cen 2005; Mason & Gronke 2020). As the neutral hydrogen fraction in the IGM increases with increasing redshift, we expect the Lyα emission lines of LAEs to become narrower and less luminous, and only the red wings of the lines to be visible. At the highest redshifts, we will no longer see the Lyα line at all, except in the most highly ionized regions of the IGM.

This evolution of the LAE population is apparent in both a drop in the normalization of the LAE luminosity function (LF) toward higher redshifts and a decrease in the LAE line widths from $z = 5$ to $z = 7$, though both of these results appear to depend on the luminosities of the LAEs (Konno et al. 2014, 2018; Santos et al. 2016; Itoh et al. 2018; Taylor et al. 2020, 2021; Goto et al. 2021; Ning et al. 2022; Songaila et al. 2022).

A similar result is seen in UV continuum samples, where the fraction of objects with strong Lyα emission appears to decline beyond $z = 6$ (Stark et al. 2010; Pentericci et al. 2018; Hoag et al. 2019). However, both the significance of this result and the redshift where the drop occurs are controversial (see, e.g., Stark 2016; Fuller et al. 2020; Kusakabe et al. 2020).

Quasar spectra support the idea of patchiness in the reionization process (e.g., Becker et al. 2015), as do other lines of evidence, such as multipeaked LAE spectra (Hu et al. 2016; Songaila et al. 2018; Bosman et al. 2020; Meyer et al. 2021) and the distribution of LAEs. As an example of the latter effect, Larson et al. (2022) found a candidate LAE at $z = 8.7$ near a known source at a similar redshift (Zitrin et al. 2015). Furthermore, we are beginning to see LAEs well into the redshift range where we would expect the IGM to be substantially neutral (e.g., Oesch et al. 2015; Zitrin et al. 2015; Hashimoto et al. 2018; Hoag et al. 2018; Pentericci et al. 2018). Indeed, with the advent of JWST, Lyα emission has now been detected out to $z = 10.60$ (GN-z11; Bunker et al. 2023).

In combination, all of these observations can be matched to models of the evolution of LAEs and used to constrain the evolution of the IGM. Extensive simulations combining sophisticated radiative transfer codes with cosmological

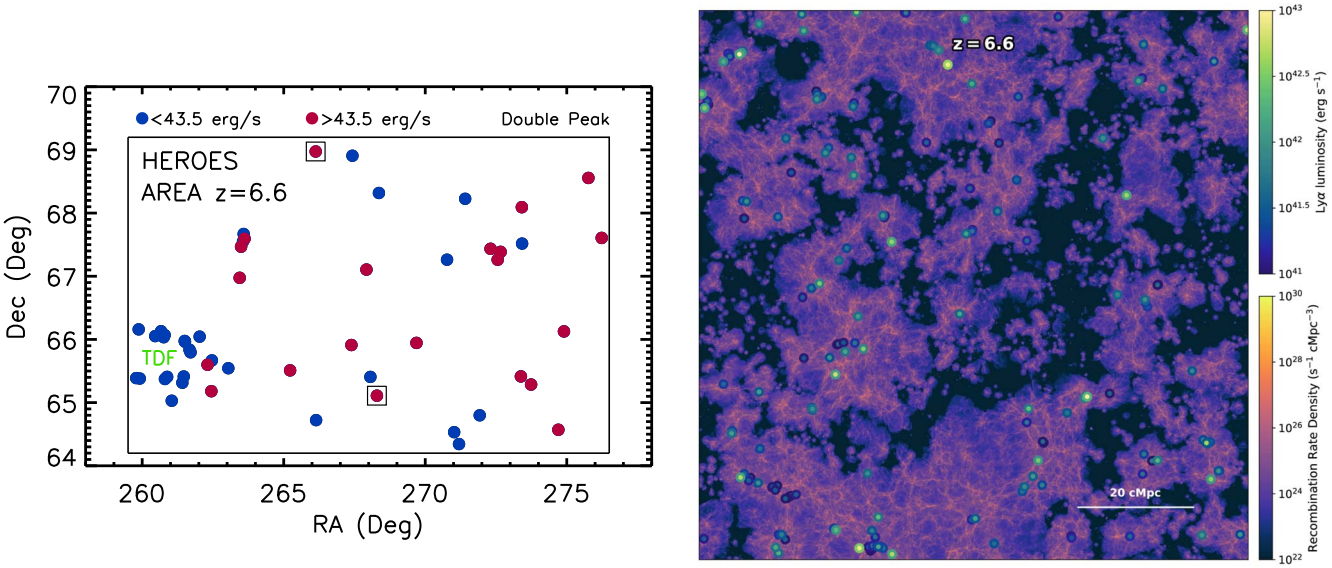

Figure 1. (Left) Positions of spectroscopically identified LAEs at $z = 6.6$ in the HEROES field (data from Taylor et al. 2023 and work in progress). The red points show the 21 sources with log $L(\mathrm{Ly}\alpha) > 43.5$ erg s^{-1}, where the sample is complete. The two sources with double-peaked spectra are marked with open squares. The sources in the lower left lie in the area around the JWST Time Domain Field (Jansen & Windhorst 2018), where our deeper HSC NB921 observations allow us to probe the lower-luminosity $z = 6.6$ LAE population (labeled TDF in green). (Right) Simulations such as THESAN (figure from Xu et al. 2023; circles show LAEs at $z = 6.6$, and purple shading shows the ionization of the IGM) are now reaching the point where we can make direct comparisons with observations of the numbers and spatial distribution of LAEs. The portion of the THESAN simulation shown is almost exactly matched in area and redshift coverage to HEROES.

models, such as THESAN (e.g., Garaldi et al. 2022; Neyer et al. 2024) and SPHINX (e.g., Garel et al. 2021; Katz et al. 2023), are now being carried out for this purpose. Despite the beautiful results from these simulations, there are still many uncertainties. Perhaps most importantly, it is not easy to disentangle the effects of the IGM from the complexity of the galaxy's Lyα emission and the scattering at circumgalactic scales (Laursen et al. 2011; Jensen et al. 2013; Garel et al. 2015; Hassan & Gronke 2021; Guo et al. 2023).

In order to model the evolution of the IGM at very high redshifts, we need to separate the effects of the IGM from the intrinsic structure of the Lyα line emerging from the galaxy and its surrounding circumgalactic medium (CGM). The simplest approach is to assume that the emergent Lyα lines are varying more slowly with redshift than the IGM properties. However, even with such a crude assumption, we must have a large reference sample to understand how the significant variations in the emergent Lyα lines (e.g., Guo et al. 2023) combine with the IGM structure to match to the observations. More sophisticated modeling also requires detailed information on large samples of LAEs to constrain the underlying assumptions. A further complication is that the line properties appear to be a function of the Lyα luminosity (e.g., Santos et al. 2016; Taylor et al. 2020, 2021; Ning et al. 2022; Songaila et al. 2022), introducing a shape dependence in the evolution of the Lyα LF and a dependence of the velocity width on the Lyα luminosity. Thus, we also need to sample a wide range of Lyα luminosities.

In practice, the highest redshift where high-quality spectra of hundreds of LAEs can be straightforwardly obtained is $z = 7$, where giant optical imagers, such as Hyper Suprime-Cam (HSC) on the Subaru 8.2 m telescope, can be used to generate narrowband-selected samples (e.g., SILVERRUSH (Konno et al. 2018) and HEROES (Taylor et al. 2023); see also the LAGER survey, which uses DECam on the CTIO Blanco 4 m telescope (Wold et al. 2022)). These can then be followed up with efficient optical spectrographs to generate large spectroscopic samples. The lowest-background long-wavelength regions in the atmospheric emission are at 8160 Å and 9210 Å, which correspond to $z = 5.7$ and $z = 6.6$; ∼100 Å filters at these wavelengths are used to make the initial selections of narrowband excess objects (see, e.g., Shibuya et al. 2018; Ning et al. 2022; Kikuta et al. 2023; Taylor et al. 2023). Ideally, the LAE samples should be complete to a limiting observed Lyα luminosity and cover large contiguous areas (10s of deg^2) in fields with extensive ancillary observations.

Our primary field is the 44 deg^2 HEROES field in the North Ecliptic Pole (NEP; Taylor et al. 2023), which has, or will have, deep coverage from the eROSITA X-ray and SPHEREx spectroscopy missions and contains the largest of the Euclid Deep Fields (20 deg^2). The goal of the present paper is to provide a publicly available atlas of uniform spectra for a very large sample of LAEs at $z = 5.7$ and $z = 6.6$ over a range of observed Lyα luminosities in this field together with a number of smaller areas. This sample can be used to characterize the LAE properties, to assess the evolution of the ionization structure, and to match to the models at these later stages in the reionization process. As an example, in Figure 1, we show the current spectroscopically confirmed LAE sample at $z = 6.6$ in HEROES, which we compare with a similarly sized area in the THESAN simulation of Lyα emission at high redshifts (Xu et al. 2023). In this simulation, the $z = 6.6$ LAEs are seen to occur in regions of the IGM that are more ionized (purple shading) and to be absent in regions that are more opaque.

We present our spectroscopic observations and discuss our observed Lyα line profiles in Section 2. In Section 3, we briefly summarize the various types of exotic LAEs seen in the sample. In Section 4, we make our Lyα line width measurements. In Section 5, we discuss the evolution of the velocity widths with redshift. Finally, in Section 6, we consider

the constraints on the IGM evolution that may be derived from the observations.

We use a $H_0 = 70$ km s^{-1} Mpc^{-1}, $\Omega_M = 0.3$, and $\Omega_\Lambda = 0.7$ cosmology throughout.

2. Observations

We have been obtaining follow-up spectroscopy of narrow-band-selected samples (using the narrowband filters NB816 for $z = 5.7$ and NB921 for $z = 6.6$) in HEROES and other fields in the Subaru/HSC and Subaru/Suprime-Cam archives. These Subaru imaging observations provide very large samples (many thousands) of photometrically selected narrowband excess sources satisfying the LAE selection criteria: NB816 $-i > 1.2$ for $z = 5.7$, with the sources also undetected in the g and r bands, and NB921 $-z > 1$ for $z = 6.6$, with the sources also undetected in the g, r, and i bands. Thus, we have many available candidates for follow-up spectroscopy. Most of these lie in small areas (5–7 deg^2). HEROES (Figure 1) is the largest contiguous field (44 deg^2) in our spectroscopic survey.

We give the observed field for each object in Tables 1, 2, and 3, along with the R.A. and decl. of each object. The selection of the sources observed prior to 2010 is summarized in Hu et al. (2010). For sources observed after 2010, we give the narrowband and continuum magnitudes in Table 3, together with cutouts of the images when these were observed with HSC. The LAEs in the NEP (52 of the $z = 6.6$ sample and 34 of the $z = 5.7$ sample) were taken from the catalog of Taylor et al. (2023). The remaining sample comes from the SSA22, XMM-LLS, COSMOS, and GOODS-N fields, all of which were observed as part of the HSC-SSP initiative (Aihara et al. 2022).

We carried out our spectroscopic observations over a very extended period from 2002 to 2023 August, but the observations were all done in a uniform fashion with the same spectrograph configuration and wavelength range. We give the date of each observation in Table 3. Hu et al. (2010) described some of the earlier spectra, and spectroscopic observations for a number of the sources have appeared in the literature (e.g., Sobral et al. 2015; Jiang et al. 2017; Matthee et al. 2017; Shibuya et al. 2018; Songaila et al. 2018, 2022).

We used the Keck/DEIMOS spectrograph with the 830 line mm^{-1} grating and 1″ slits, which gives good red sensitivity and moderately high resolution. Because of ghosting in this configuration, we used three dithered 20 minutes observations. The total exposure time is 1 hr for most of the sources. Some LAEs have multiple observations and hence longer exposure times. The total exposure time for each source may be found in Table 3. Because the sources are sparse, there are usually only one or two LAEs in each DEIMOS mask. The data reduction is described in Cowie et al. (1996). We measure the instrumental resolution from the sky lines, giving an average of 85 km s^{-1} at $z = 6.6$ and 96 km s^{-1} at $z = 5.7$.

We summarize the LAE targets and the fields they are drawn from in Tables 1 ($z = 5.7$) and 2 ($z = 6.6$). We give the signal-to-noise of the LAEs in Table 3.

On average, the LAEs at these high redshifts have a very generic (and well-known) spectral shape, with a sharp break at the blue side and a tail to the red side (see Figure 2). The small number of low-redshift contaminants of the narrowband candidate sources (∼5%) are easily recognized by the doublet nature of the [O II]3727 and [O III]5007 lines and were dropped from the sample. A larger number of the narrowband-selected sources (∼25%) were not confirmed by the spectroscopy and were also eliminated. The weak continuum also shows the break at the Lyα wavelength. We see very little change in the shape and width of the average Lyα line profile between $z = 5.7$ and $z = 6.6$. The shape is governed by the escape of Lyα from the galaxy and its circumgalactic gas, combined with the blue-side scattering from the neutral IGM. (See Guo et al. 2023 and references therein for an extensive recent discussion.)

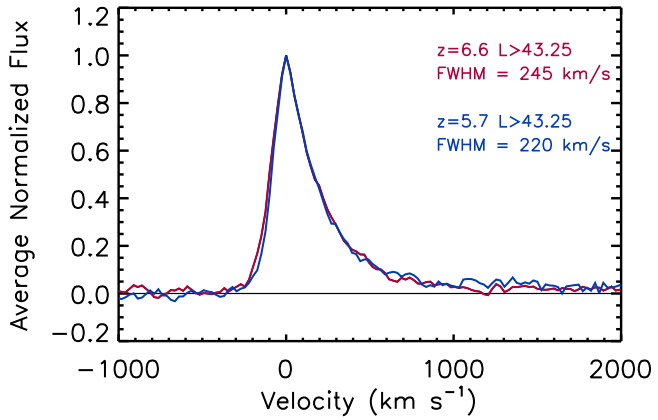

Figure 2. Average normalized Lyα spectra for luminous LAEs (log L(Lyα) >43.25 erg s^{-1}) at $z = 5.7$ (blue; 55 objects) and $z = 6.6$ (red; 57 objects). The FWHM of the stacked spectra at the two redshifts are shown. The spectra are from the 830 line mm^{-1} grating on the Keck/DEIMOS spectrograph. The instrumental FWHM of 85 km s^{-1} at $z = 6.6$ and 96 km s^{-1} at $z = 5.7$ are not subtracted here.

However, these average line profiles are, in reality, drawn from a fairly diverse set of individual line shapes and widths, as we illustrate in Figure 3, where we show two-dimensional (2D) spectra for a subset of our $z = 5.7$ LAEs. We see objects with a wide range of red velocity wings, including some spectacularly long-tailed objects, such as sources 4 and 69. We also see objects with blue emission relative to the Lyα peak, such as source 2, and lensed systems, such as source 114. This variety reflects the variation in the redshift of the galaxy with respect to the local IGM, the variation in the ionization surrounding the source, and the degree to which escaping from the galaxy and the CGM has moved the emission to the red.

3. Exotic LAEs

As mentioned above, our large LAE spectroscopic samples allow us to find rare and interesting objects. In general, only one to a few of these have been found, emphasizing the need to continue to increase the numbers in our spectroscopically observed sample so we can find further examples and make statistical use of them. We describe three categories of such exotic LAEs here.

3.1. Double-peaked LAEs

While double-peaked Lyα profiles resulting from the escape of the line from the galaxy and the CGM are seen in ∼30% of low- to moderate-redshift LAEs (e.g., Kulas et al. 2012), at high redshifts, we expect any blue wing to be removed by scattering in the IGM. However, we see a handful of LAEs with blue-side emission (e.g., Hu et al. 2016; Songaila et al. 2018; Bosman et al. 2020; Meyer et al. 2021 for published examples). We show a double-peaked LAE in Figure 4, which we compare with a single-peaked LAE of similar luminosity.

Table 1
$z = 5.7$ Lyα Sample

Field	R.A.	Decl.	z	log L(Lyα) (erg s^{-1})	FWHM (km s^{-1})	Error (km s^{-1})	$a_{\rm asym}$	Error
XMM-LSS	33.86914	−4.81525	5.7166	43.48	414.61	25.47	0.26	0.02
XMM-LSS	34.10295	−4.92128	5.7050	43.41	305.15	36.75	0.10	0.06
XMM-LSS	34.35014	−5.55270	5.7060	43.53	242.08	11.97	0.31	0.01
XMM-LSS	34.65159	−5.59116	5.6973	43.39	188.88	16.98	0.41	0.02
XMM-LSS	35.35540	−3.67684	5.6982	43.56	578.22	58.60	0.46	0.04
XMM-LSS	35.35643	−4.13690	5.6760	43.47	253.17	16.14	0.26	0.02
XMM-LSS	35.94127	−3.90492	5.7360	43.28	260.58	11.62	0.16	0.02
XMM-LSS	35.49671	−4.97522	5.6968	43.37	288.28	18.04	0.08	0.03
A370	39.97289	−1.60773	5.6933	42.85	270.70	22.31	0.17	0.04
A370	40.06517	−1.49633	5.7122	42.90	390.72	38.96	0.17	0.04
A370	40.12097	−1.65553	5.6437	42.95	381.85	53.90	0.06	0.07
A370	40.13245	−1.54178	5.7126	42.57	296.97	63.04	0.15	0.10
A370	40.14673	−1.60750	5.6831	42.87	242.36	46.98	0.48	0.04
A370	40.16127	−1.58338	5.7080	42.77	228.42	20.07	0.27	0.03
A370	40.17686	−1.55455	5.6561	42.85	262.02	37.95	0.10	0.07
A370	40.23523	−1.47936	5.7078	42.79	302.47	25.76	0.33	0.03
A370	40.24645	−1.46045	5.7300	42.89	292.69	25.77	0.31	0.03
A370	40.26759	−1.46400	5.7310	42.88	404.41	31.62	0.20	0.03
A370	40.34016	−1.53909	5.6789	42.79	214.26	20.64	0.05	0.05
GOODS-N	188.76352	62.28720	5.6985	43.04	302.82	30.51	0.23	0.03
GOODS-N	188.81929	62.08558	5.7220	42.77	74.86	15.23	0.38	0.03
GOODS-N	188.88393	62.24594	5.7026	42.57	134.96	47.57	0.41	0.06
GOODS-N	188.99542	62.17142	5.6733	42.58	168.20	88.07	0.53	0.09
GOODS-N	189.03284	62.14396	5.6406	42.95	354.87	23.31	0.15	0.03
GOODS-N	189.03906	62.04567	5.7200	42.72	274.77	46.38	0.35	0.05
GOODS-N	189.05014	62.07235	5.7410	42.82	263.38	36.40	0.01	0.07
GOODS-N	189.05605	62.13004	5.6350	42.95	269.44	34.37	0.31	0.04
GOODS-N	189.21527	62.32684	5.6763	42.96	349.14	33.95	0.06	0.05
GOODS-N	189.21686	62.36461	5.6890	42.92	255.62	19.77	0.12	0.04
GOODS-N	189.32457	62.29978	5.6630	42.91	254.76	33.77	0.31	0.04
GOODS-N	189.43633	62.19595	5.6753	43.26	447.39	57.51	0.28	0.05
GOODS-N	189.48480	62.40435	5.6486	42.60	220.31	35.71	0.18	0.07
GOODS-N	189.57741	62.27264	5.7275	43.55	360.75	57.98	0.18	0.07
GOODS-N	189.59084	62.17962	5.6490	42.83	348.24	74.42	0.28	0.07
GOODS-N	189.64726	62.11198	5.6940	42.80	122.23	30.11	0.30	0.07
GOODS-N	189.76289	62.24575	5.7374	43.07	225.27	26.14	0.32	0.03
GOODS-N	189.97046	62.17626	5.6356	42.98	330.55	33.84	0.31	0.03
GOODS-N	190.03114	62.21266	5.7388	42.74	254.66	19.55	0.23	0.03
GOODS-N	190.06612	62.29416	5.6945	42.57	455.95	89.96	0.14	0.09
GOODS-N	190.13959	62.31078	5.6502	43.15	320.44	29.03	0.18	0.04
GOODS-N	190.18228	62.25968	5.7055	42.84	179.52	27.65	0.42	0.03
GOODS-N	190.26646	62.36457	5.7437	42.94	329.14	26.64	0.11	0.04
GOODS-N	190.28117	62.38783	5.6865	42.66	222.16	22.44	0.17	0.04
GOODS-N	190.31573	62.38276	5.7020	43.18	325.04	34.85	0.31	0.03
GOODS-N	190.35735	62.34753	5.7154	43.17	278.10	20.62	0.36	0.02
GOODS-N	190.36993	62.33969	5.6960	43.44	290.44	5.24	0.34	0.01
GOODS-N	190.47531	62.41094	5.7458	42.82	228.14	12.95	0.33	0.02
SSA17	256.56177	43.80437	5.6655	42.70	367.82	81.64	0.02	0.11
SSA17	256.69565	43.75570	5.7116	42.88	387.66	64.12	0.12	0.08
SSA17	256.70090	43.97053	5.7275	42.95	290.28	20.51	0.33	0.02
SSA17	256.73926	43.77398	5.6626	42.86	299.08	42.69	0.39	0.04
SSA17	256.76758	43.96976	5.7012	42.74	255.60	33.75	0.11	0.06
SSA17	256.78308	43.92512	5.7010	42.67	336.17	77.82	0.25	0.08
NEP	259.37943	66.38524	5.7009	43.53	205.13	8.95	0.26	0.01
NEP	261.13239	66.46720	5.6637	43.86	201.86	21.97	0.25	0.04
NEP	261.20316	65.01511	5.7403	43.48	249.22	15.50	0.29	0.02
NEP	261.61444	66.34655	5.6528	44.03	271.17	11.50	0.32	0.01
NEP	262.36450	68.03432	5.7407	43.65	333.23	25.22	0.36	0.02
NEP	263.36462	68.19836	5.6957	43.48	354.00	18.06	0.33	0.02
NEP	263.44412	66.33298	5.7183	43.30	294.91	42.52	0.42	0.04
NEP	265.63666	68.49759	5.7182	43.46	264.59	32.90	0.17	0.05
NEP	266.47528	67.92089	5.7040	43.39	270.96	20.63	0.26	0.03
NEP	266.61945	68.01823	5.6766	43.60	250.38	17.25	0.27	0.02
NEP	267.68088	66.89002	5.7230	43.57	478.16	30.16	0.24	0.03

Table 1
(Continued)

Field	R.A.	Decl.	z	log L(Lyα) (erg s^{-1})	FWHM (km s^{-1})	Error (km s^{-1})	$a_{\rm asym}$	Error
NEP	267.78796	66.72775	5.6963	43.49	228.42	14.40	0.22	0.02
NEP	267.89209	66.62925	5.6919	43.79	505.31	43.65	0.23	0.04
NEP	268.73529	64.31248	5.7280	43.46	261.79	25.72	0.26	0.03
NEP	268.74176	64.24213	5.6950	43.45	439.56	36.47	0.18	0.04
NEP	270.15982	68.81596	5.6950	43.51	369.43	77.10	0.37	0.07
NEP	270.65686	67.81599	5.7192	43.49	477.36	26.28	0.31	0.02
NEP	270.96326	68.07949	5.7250	43.55	143.85	6.06	0.09	0.02
NEP	271.01611	67.01797	5.7134	43.49	307.07	27.84	0.34	0.03
NEP	271.33987	67.92043	5.7210	43.85	424.59	10.94	0.07	0.01
NEP	271.72308	64.85684	5.7061	43.31	228.82	19.48	0.32	0.02
NEP	271.95343	64.92245	5.7225	43.56	239.24	17.53	0.38	0.02
NEP	272.35791	64.83362	5.7017	43.29	540.57	23.53	0.50	0.02
NEP	272.41608	66.77439	5.7448	43.48	308.91	24.75	0.25	0.03
NEP	272.58472	66.69049	5.7350	43.70	408.68	11.76	0.16	0.01
NEP	273.02316	68.85086	5.7222	43.66	244.17	12.41	0.35	0.01
NEP	273.24777	69.00883	5.6995	43.25	266.41	21.12	0.12	0.04
NEP	274.18512	66.97318	5.7570	43.78	309.06	8.89	0.16	0.01
NEP	274.55298	67.84969	5.7225	43.51	329.60	17.77	0.22	0.02
NEP	274.67450	64.77733	5.7218	43.44	232.47	17.02	0.35	0.02
NEP	274.79449	66.03417	5.7252	43.32	262.44	18.34	0.01	0.04
NEP	275.87070	64.56598	5.7356	43.46	282.88	18.30	0.28	0.02
NEP	276.02689	64.44939	5.7170	43.42	326.69	31.89	0.17	0.04
NEP	276.66409	67.53183	5.7120	43.50	233.28	11.32	0.13	0.02
SSA22	333.67297	−0.26941	5.7119	43.55	185.01	4.87	0.09	0.01
SSA22	333.80704	−0.49459	5.6955	43.51	262.84	17.19	0.27	0.02
SSA22	334.22006	0.27775	5.6620	42.82	328.94	67.59	0.39	0.06
SSA22	334.22888	0.09408	5.6849	43.15	364.20	18.39	0.11	0.02
SSA22	334.23529	0.24630	5.6621	42.98	357.54	75.48	0.29	0.07
SSA22	334.24414	0.14338	5.7378	42.76	128.70	30.67	0.42	0.04
SSA22	334.24490	0.31372	5.6388	42.93	425.33	81.10	0.07	0.10
SSA22	334.27319	0.21692	5.6703	42.97	327.40	33.94	0.29	0.04
SSA22	334.27838	0.20631	5.6510	42.88	276.59	65.45	0.21	0.09
SSA22	334.28033	0.46247	5.7256	42.91	304.47	58.97	0.40	0.06
SSA22	334.29242	0.21128	5.6260	43.27	429.34	163.08	0.39	0.13
SSA22	334.31812	0.22382	5.6473	43.05	585.18	75.49	0.34	0.05
SSA22	334.33691	0.33536	5.6706	43.06	167.61	26.74	0.27	0.05
SSA22	334.33722	0.29383	5.6672	43.15	460.95	36.95	0.18	0.04
SSA22	334.35437	0.13128	5.7529	42.93	277.19	18.98	0.20	0.03
SSA22	334.36969	0.32172	5.6464	43.27	259.57	25.43	0.39	0.03
SSA22	334.38171	0.16032	5.6864	42.86	237.16	32.08	0.17	0.06
SSA22	334.38794	0.37132	5.6547	43.09	204.10	18.29	0.24	0.03
SSA22	334.38995	0.70059	5.6190	43.20	310.84	47.76	0.30	0.05
SSA22	334.41321	0.42923	5.7081	42.95	382.31	56.78	0.03	0.08
SSA22	334.42044	0.40416	5.6350	43.05	318.90	31.73	0.21	0.04
SSA22	334.43582	0.67348	5.6860	42.54	333.26	50.19	0.06	0.08
SSA22	334.46979	0.60430	5.7330	42.84	253.51	21.37	0.12	0.04
SSA22	334.47122	1.11505	5.7216	43.28	200.83	16.17	0.17	0.04
SSA22	334.48886	0.68858	5.6870	42.47	215.00	49.41	0.19	0.09
SSA22	334.50912	0.24213	5.6748	43.08	235.74	21.64	0.28	0.03
SSA22	334.51050	0.50208	5.6613	42.53	375.30	75.73	0.32	0.07
SSA22	334.53766	1.12323	5.7493	43.87	165.53	6.00	0.33	0.01
SSA22	334.54785	0.08356	5.7101	43.15	183.79	12.40	0.29	0.02
SSA22	334.55170	0.72510	5.6450	42.70	293.85	54.95	0.24	0.07
SSA22	334.56860	0.61319	5.7324	42.86	205.64	21.65	0.20	0.04
SSA22	334.63617	0.47907	5.6820	43.20	250.56	10.25	0.33	0.01
SSA22	334.67990	0.74419	5.6560	43.10	175.20	14.57	0.31	0.02
SSA22	334.69003	0.56826	5.6939	42.67	256.90	27.31	0.23	0.04
SSA22	334.69302	0.53241	5.6409	42.70	213.64	24.55	0.16	0.05
SSA22	334.76755	0.42243	5.6271	42.96	225.34	79.33	0.42	0.08
SSA22	334.79910	−0.51076	5.7060	43.47	205.21	10.66	0.29	0.02
SSA22	334.87347	−0.93630	5.6925	43.31	250.80	22.17	0.27	0.03
SSA22	334.89648	−0.78148	5.7120	43.49	206.60	12.93	0.29	0.02
SSA22	335.85464	−0.69387	5.7325	43.25	154.78	33.14	0.15	0.10

Table 2
$z = 6.6$ Lyα sample

Field	R.A.	Decl.	z	log L(Lyα)	FWHM	Error	$a_{\rm asym}$	Error
				(erg s^{-1})	(km s^{-1})			
XMM-LSS	35.90345	−3.93370	6.5473	43.44	310.06	29.76	0.30	0.03
XMM-LSS	36.09813	−4.00951	6.5634	43.61	137.78	4.80	0.27	0.01
A370	39.86338	−1.58983	6.4504	42.73	193.09	20.84	0.22	0.04
A370	39.91438	−1.57567	6.5409	42.76	189.52	30.17	0.36	0.04
A370	39.91479	−1.58100	6.5299	42.90	160.02	16.38	0.39	0.02
A370	39.95666	−1.52267	6.5637	42.99	221.76	21.91	0.26	0.03
A370	39.97811	−1.55897	6.5590	43.41	227.72	18.59	0.27	0.03
A370	40.00753	−1.68339	6.5428	42.72	182.81	39.16	0.33	0.06
A370	40.01770	−1.38128	6.5029	42.62	112.83	40.04	0.40	0.06
A370	40.22926	−1.72099	6.4803	42.91	300.34	49.29	0.29	0.05
A370	40.39424	−1.61179	6.4693	42.86	233.36	37.70	0.24	0.06
COSMOS	150.24178	1.80411	6.6038	43.67	268.10	9.64	0.29	0.01
COSMOS	150.35336	2.52924	6.5439	43.42	277.37	19.17	0.30	0.02
COSMOS	150.64742	2.20389	6.5922	43.70	248.72	10.93	0.24	0.01
GOODS-N	189.35826	62.20772	6.5593	43.45	188.57	11.81	0.22	0.02
GOODS-N	190.00757	62.32957	6.5126	42.88	215.25	67.43	0.28	0.10
GOODS-N	190.56474	62.29151	6.5198	42.94	241.91	62.82	0.42	0.06
SSA17	256.81799	43.84443	6.5273	43.29	299.31	34.08	0.31	0.04
NEP	259.78857	65.38805	6.5773	43.30	386.01	49.29	0.38	0.04
NEP	259.91315	65.38100	6.5752	43.45	267.95	13.11	0.21	0.02
NEP	260.66571	66.13013	6.5791	43.08	289.71	43.88	0.24	0.06
NEP	260.79163	66.06917	6.5942	43.29	233.49	21.93	0.33	0.03
NEP	260.80258	65.37336	6.5815	43.48	309.97	19.40	0.22	0.02
NEP	260.88062	65.40775	6.5465	43.20	211.06	25.96	0.20	0.05
NEP	261.67026	65.83727	6.5496	43.17	228.97	27.98	0.17	0.05
NEP	261.70859	65.79610	6.5617	43.40	361.73	31.45	0.24	0.03
NEP	262.02902	66.04409	6.5997	43.27	371.20	55.51	0.23	0.06
NEP	262.30841	65.59969	6.5689	43.64	312.69	20.71	0.38	0.02
NEP	262.44296	65.18044	6.5670	43.78	388.33	20.24	0.27	0.02
NEP	262.46060	65.66861	6.5658	43.05	174.93	22.76	0.30	0.04
NEP	263.61490	67.59397	6.5839	43.67	213.45	8.24	0.35	0.01
NEP	265.22437	65.51039	6.5989	43.67	237.56	5.36	0.27	0.01
NEP	266.12918	68.97475	6.5849	43.61	184.97	14.65	0.28	0.02
NEP	266.14337	64.72261	6.5790	43.47	286.98	43.97	0.43	0.04
NEP	267.42700	68.90741	6.5500	43.47	275.83	15.01	0.23	0.02
NEP	268.29211	65.10958	6.5471	43.75	248.38	15.15	0.36	0.02
NEP	269.68964	65.94475	6.5363	43.60	334.20	25.74	0.26	0.03
NEP	271.92371	64.79888	6.5501	43.37	256.95	22.12	0.31	0.03
NEP	272.30804	67.43481	6.5823	43.52	248.60	18.66	0.15	0.03
NEP	272.55881	67.26176	6.5998	43.60	342.52	25.48	0.38	0.02
NEP	272.66104	67.38605	6.5784	43.59	339.27	26.18	0.39	0.02
NEP	273.41190	68.09296	6.5777	43.52	170.53	14.79	0.24	0.03
NEP	273.42078	67.51686	6.5542	43.50	350.14	26.68	0.21	0.03
NEP	273.73837	65.28600	6.5795	43.94	284.99	5.88	0.35	0.01
NEP	274.70264	64.57021	6.5728	43.55	262.56	23.37	0.29	0.03
NEP	274.90005	66.12672	6.5337	43.53	376.99	30.79	0.20	0.03
NEP	275.76389	68.55573	6.5504	43.52	264.44	20.89	0.32	0.02
NEP	276.23428	67.60670	6.5354	43.63	287.57	26.00	0.31	0.03
SSA22	333.68112	−0.57300	6.5582	43.33	266.45	26.02	0.36	0.03
SSA22	334.40994	0.15267	6.4850	42.87	183.14	35.76	0.03	0.10
SSA22	334.42136	0.52625	6.5019	43.28	337.11	35.64	0.22	0.04
SSA22	334.42929	0.30240	6.4702	43.20	254.62	28.63	0.10	0.06
SSA22	334.50800	0.81224	6.5178	42.60	172.83	15.16	0.23	0.03
SSA22	334.59787	0.77540	6.4841	42.90	216.00	31.12	0.30	0.04
SSA22	334.61520	0.79093	6.5051	43.05	219.20	25.58	0.15	0.05
SSA22	334.70264	0.73160	6.5212	42.95	186.10	33.50	0.36	0.04
SSA22	334.73483	0.13537	6.5149	43.69	309.41	19.79	0.34	0.02
SSA22	334.74216	0.76499	6.5556	42.81	206.76	38.15	0.26	0.06
NEP	259.87549	66.15894	6.5878	43.39	219.92	16.78	0.25	0.03
NEP	260.45947	66.05280	6.5984	43.21	368.14	86.91	0.47	0.07
NEP	260.75922	66.03492	6.5937	43.00	214.71	52.50	0.36	0.06
NEP	261.04294	65.02969	6.5766	43.33	339.90	48.69	0.24	0.05
NEP	261.41815	65.31500	6.5875	43.28	191.76	189.94	0.62	0.19

Table 2
(Continued)

Field	R.A.	Decl.	z	log L(Lyα) (erg s^{-1})	FWHM (km s^{-1})	Error (km s^{-1})	$a_{\rm asym}$	Error
NEP	261.46747	65.41328	6.5930	43.17	198.52	20.60	0.14	0.05
NEP	261.50146	65.97598	6.5942	43.30	161.14	14.80	0.27	0.03
NEP	261.51166	65.96345	6.5635	43.14	323.21	82.15	0.26	0.09
NEP	263.04303	65.54397	6.6018	43.37	263.27	36.18	0.28	0.04
NEP	263.44409	66.97511	6.6176	43.71	284.68	18.66	0.30	0.02
NEP	263.49301	67.46775	6.5584	43.53	400.64	73.07	0.32	0.06
NEP	263.56140	67.55155	6.5502	43.32	215.68	23.62	0.31	0.03
NEP	263.58398	67.66872	6.5586	43.47	190.15	20.40	0.25	0.04
NEP	267.39105	65.91167	6.5355	43.52	261.90	11.41	0.29	0.01
NEP	268.06177	65.40675	6.5856	43.45	186.88	15.72	0.25	0.03
NEP	268.36270	68.31772	6.5973	43.46	254.98	17.53	0.28	0.02
NEP	270.76889	67.26186	6.5456	43.49	230.67	28.02	0.36	0.03
NEP	271.02075	64.53217	6.5989	43.39	213.44	15.63	0.24	0.03
NEP	271.19232	64.34397	6.5587	43.45	224.26	19.92	0.29	0.03
NEP	273.37930	65.41480	6.5509	43.56	320.28	20.99	0.28	0.02
XMM-LSS	35.58046	−3.53547	6.5556	43.48	295.70	30.37	0.28	0.03
NEP	267.92221	67.10558	6.6283	43.61	196.23	26.66	0.34	0.04
NEP	271.40976	68.22611	6.6165	43.46	226.94	62.48	0.36	0.07
SSA22	334.90829	−0.07106	6.6038	43.55	317.08	18.07	0.32	0.02

Table 3
Spectral Atlas Contents

1	Field
2	Previous Name
3	Current Name
4, 5	J2000.0 R.A. and decl. of LAE
6	Redshift of LAE peak
7	Wavelength vector (Å)
8	Spectrum vector
9	Observed Lyα luminosity (erg s^{-1})
10	2D spectral image centered on Lyα line
11	Wavelength for 2D spectral image (Å)
12	Spectrum corresponding to 2D spectral image
13	Velocity centered on Lyα peak corresponding to 2D spectral image (km s^{-1})
14	Sky vector corresponding to 2D spectral image
15, 16	FWHM and error (km s^{-1})
17, 18	Asymmetry parameter ($a_{\rm asym}$) and error
19, 20	Peak amplitude (A) and error
21, 22	Width parameter (d) and error
23	Double-peaked LAE flag (1 = single, 2 = double)
24	Exposure time (hr)
25	Date of observation
26–28	15″ cutout image NB816, z, i ($z = 5.7$); NB921, y, z ($z = 6.6$)
29–32	2″ aperture mags NB816, i, z, y ($z = 5.7$); NB921, i, z, y ($z = 6.6$)

(This table is available in its entirety in FITS format.)

Double-peaked Lyα emission may be direct evidence for large ionized bubbles around these high-redshift LAEs, which may reveal reionization in progress. In this interpretation, we are seeing the Lyα profile emerging from the galaxy directly without scattering by the IGM. However, we must also consider the possibility that double-peaked Lyα profiles could result from processes other than ionized bubbles. Matthee et al. (2018) suggested that they could be the result of a merger, where both galaxies are producing Lyα lines redward of the IGM cutoff but with different velocities. This could then result in an observed double-peaked structure with different components in the LAE having significantly different redshifts.

3.2. Extended Red Wing LAEs and AGNs

As we noted in Section 2, we see a small number of LAEs with very extended red wings, in some cases to velocities beyond 2000 km s^{-1}. Yang et al. (2014) previously discussed extended red wings, but the object they considered only extends to 1000 km s^{-1}. The present sample contains much more extreme objects. The $z = 5.7$ sample contains 3 sources (4, 45, and 69) with tails extending beyond 1500 km s^{-1}. At $z = 6.6$, there are two such sources (35 and 43). Source 35 is also the double-peaked source NEPLA4.

There are also two active galactic nuclei (AGNs) in the $z = 6.6$ redshift range (Figure 5, right panel; see also Figure 11) and one in the $z = 5.7$ range. These sources are not included in the LAE samples.

In Figure 5 (left panel), we show the spectrum of one of the extended red wing LAEs (source 4 in the $z = 5.7$ sample). In addition to a narrow component, the spectrum shows a red wing extending to beyond 3000 km s^{-1}. It is difficult to reproduce such extreme line widths with models of the Lyα escape from star-forming galaxies. One possible alternative interpretation is that we are seeing a combination of narrow Lyα emission from the galaxy and broad Lyα emission from an AGN in the galaxy. These sources might be related to JWST-detected AGNs at these redshifts, some of which also show narrow lines with underlying broad components, but in the rest-frame optical (Harikane et al. 2023; Kocevski et al. 2023; Greene et al. 2024).

3.3. Lensed LAEs

Lensed LAEs are of particular interest, since the differential paths allow us to probe for the presence of small-scale structure in the circumgalactic and intergalactic gas. So far, we have only

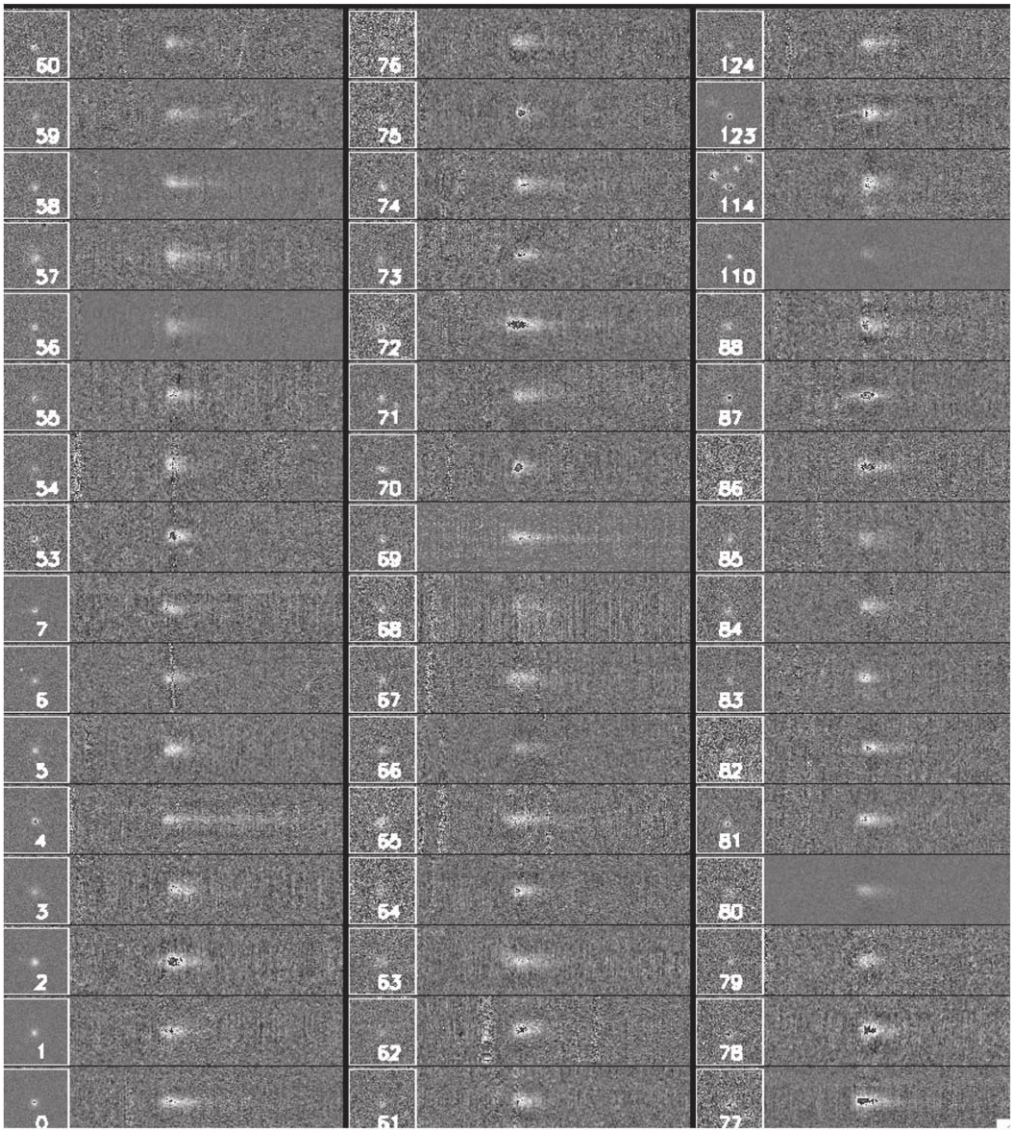

Figure 3. A subset of our existing LAE spectra at $z = 5.7$. We show a narrowband image thumbnail for each LAE (numbered), along with its 2D spectrum, where the x-axis corresponds to the wavelength and the y-axis corresponds to the spatial position along the slit. The x-axis is 140 Å long, and the y-axis is $7\farcs2$.

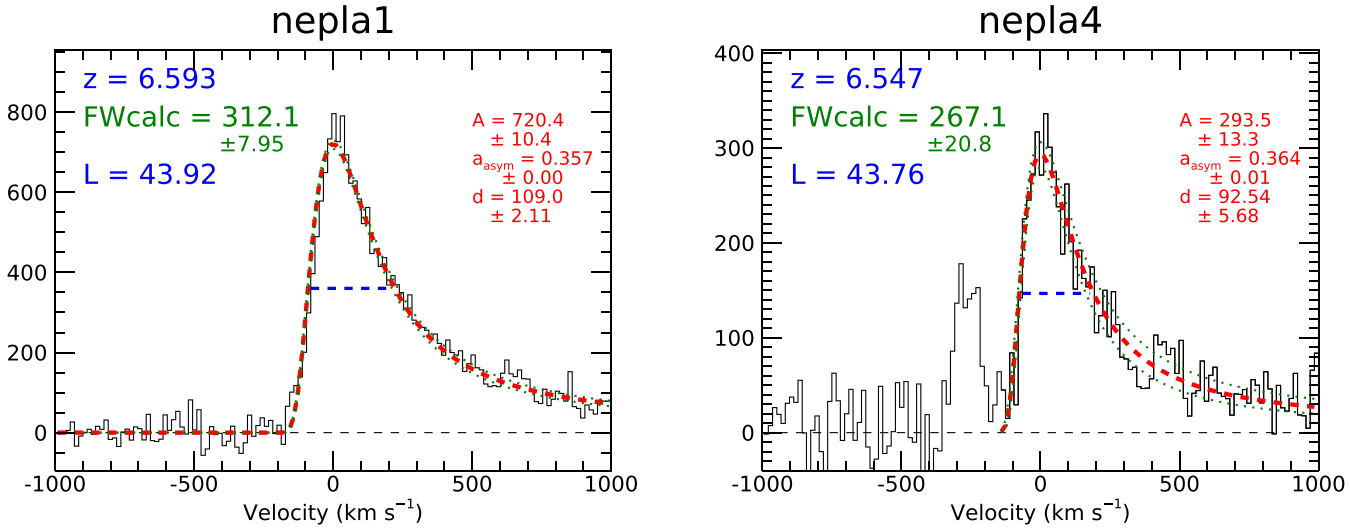

Figure 4. Asymmetric fits from Section 4 for two sources in HEROES (left: NEPLA1, a single-peaked LAE; right: NEPLA4, a double-peaked LAE, where the second peak is blueward of the principal Lyα peak). The red dashed line shows the fit to the data (black). The FWHM in km s^{-1} based on the fit is given in green and shown as the blue dashed line. The redshift and log L(Lyα) are given in blue, and the fitting parameters from Equation (1) in red. The y-axis shows the flux in arbitrary units.

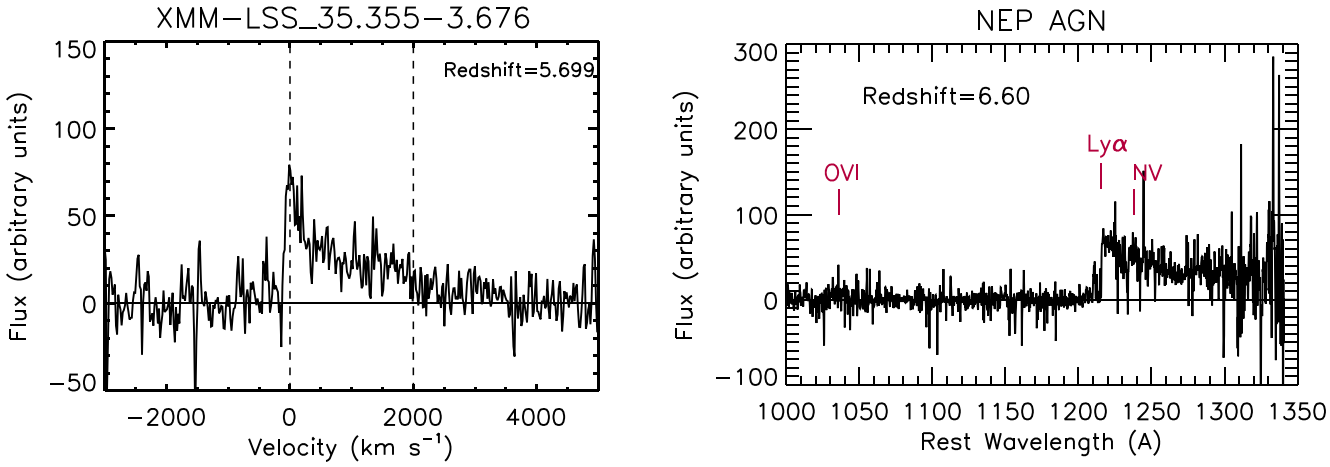

Figure 5. (Left) An LAE with an extended red wing. In addition to a narrow line, the red wing extends to ∼3000 km s^{-1}. The dashed lines show zero velocity and 2000 km s^{-1}. (Right) A broad-line AGN detected in the Lyα selected sample.

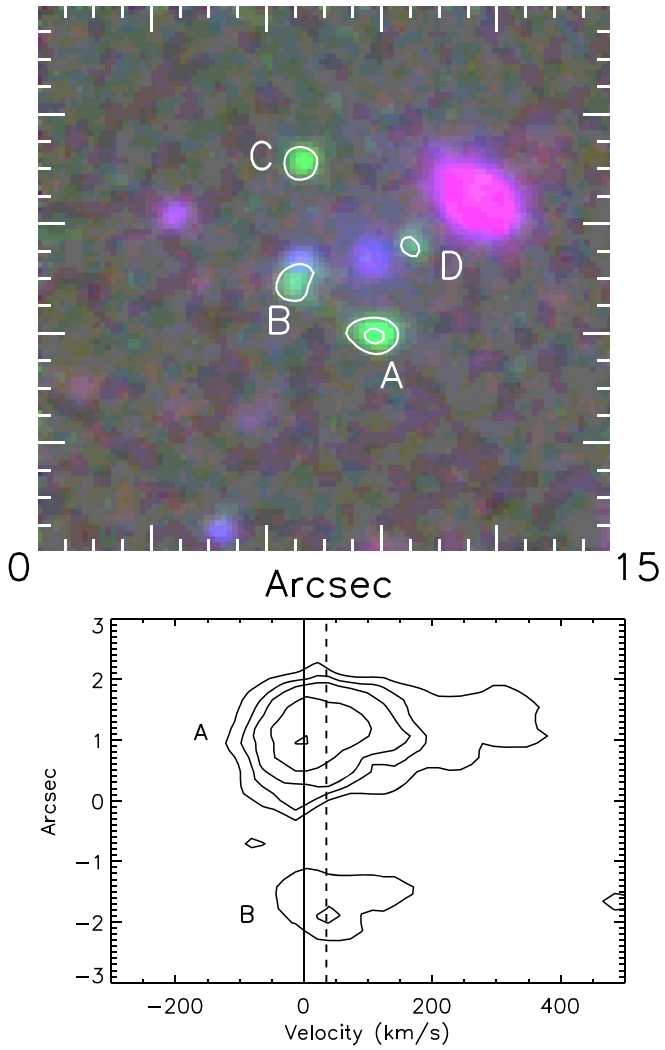

Figure 6. Upper panel: Structure of a $z = 5.749$ lensed LAE in the SSA22 field. Green indicates Lyα emission based on NB816 imaging from Subaru/HSC. For the remaining galaxies, blue shows the r band and red shows the z band. The differential paths allow us to investigate the small-scale structure in the CGM and IGM. Lower panel: Two-dimensional spectra from a slit covering components B and A. The x-axis corresponds to the velocity relative to the peak of component A. The solid line shows zero velocity, and the dashed line shows 35 km s^{-1}, which corresponds to the peak of component B.

found one such object: an LAE cross at $z = 5.749$ in the SSA22 field (see Figure 6, upper panel). The components of the cross lie at separations from 2.″5 to 5.″2, and while the components with measured redshifts (A and B) lie at similar redshifts, their Lyα profiles are not identical. Thus, as we show in Figure 6 (lower panel), component B is slightly (but significantly) redward of component A by ∼35 km s^{-1}. These changes in the Lyα profiles may reflect changes in the Lyα scattering for scales of order 10 pc in the CGM to several hundred parsecs in the IGM. The variations in the Lyα profiles should provide constraints on the modeling of LAEs and on how the profiles change with viewing angle (Guo et al. 2023).

We will consider the double-peaked sources further in the discussion, but we postpone consideration of the extended red wing sources and the LAE cross to subsequent papers.

4. Lyα Line Width Measurements

For each LAE, we first determine the redshift corresponding to the peak of the Lyα line. We then make a parameterized fit to determine the full width at half maximum (FWHM) in velocity. This gives an accessible measurement of the properties of the LAE and allows for a simple classification.

Following Shibuya et al. (2014) and Claeyssens et al. (2019), we fit the Lyα line with an asymmetric Gaussian profile,

$$f(\Delta v) = A \exp\left(-\frac{\Delta v^2}{2(a_{\rm asym}(\Delta v) + d)^2}\right), \quad (1)$$

where A is the amplitude (normalization), and Δv is the velocity relative to the peak of the Lyα profile. Here, $a_{\rm asym}$ controls the asymmetry and d controls the line width. In terms of these free parameters, the width of the line (in km s^{-1}) is

$$\mathrm{FWHM} = \frac{2\sqrt{2\ln 2}\ d}{(1 - 2\ln 2\ a_{\rm asym}^2)}. \quad (2)$$

For the double-peaked sources, we fit only to the red wing of the LAE (right panel of Figure 4).

As can be seen from the two examples shown in Figure 4, the asymmetric fit generally provides an extremely good representation of the line. At both redshifts, all of the asymmetry parameters are positive, corresponding to the wings being red. The median asymmetry parameter is 0.26 at $z = 5.7$

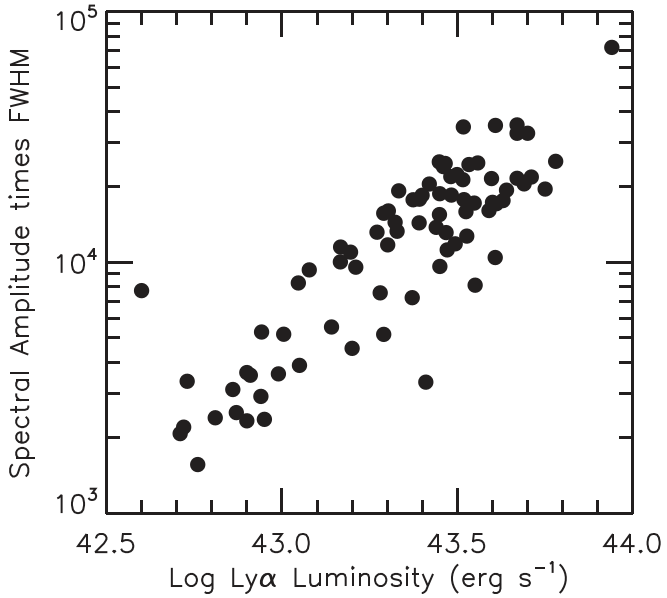

Figure 7. Comparison of the spectral line strength as measured by $A \times$ FWHM vs. L(Lyα) for the $z = 6.6$ LAEs. Only sources with measured signal-to-noise > 5 in the amplitude are shown.

and 0.28 at $z = 6.66$, and the denominator in Equation (2) increases the FWHM by ∼10%, on average. The corresponding error in the FWHM is nearly fully dominated by the error in d, with only a few percent contribution from the a_{asym} term. We tabulate the redshifts, Lyα luminosities, FWHM, and asymmetry parameters in Tables 1 and 2.

We next calculate the Lyα line fluxes and luminosities. Because of the difficulty of an absolute calibration for slit spectra, we calculate the Lyα line fluxes from the narrowband imaging. We assume that the narrowband flux is solely produced by the Lyα line. We do not correct for the continuum, which is extremely weak for these objects and not always measurable. The mean observed-frame Lyα equivalent width (EW) in the stacked normalized spectra is 600 Å at $z = 6.6$ and 410 Å at $z = 5.7$, while our selection chooses LAEs with observed-frame Lyα EWs of 130 Å or greater. Even for these lowest-EW objects, the continuum correction to the luminosities is <0.1 dex (Taylor et al. 2021). We use aperture-corrected 2″ diameter aperture magnitudes, with the correction (∼0.30 mag) determined via comparison with 4″ diameter apertures. We next divide the fluxes corresponding to the narrowband magnitudes by the filter transmission efficiencies at the spectroscopic redshifts to obtain our final Lyα line fluxes. We then determine the Lyα luminosities, L(Lyα), using the luminosity distances for our adopted cosmological geometry.

As a check, we compare our narrowband-derived L(Lyα) to our measured $A \times$ FWHM, which is roughly the spectral line strength. As can be seen from Figure 7, there is a near-linear relation between the two, which gives us confidence in our L(Lyα) measurements.

We plan on releasing an atlas of our LAE spectra on a regular basis as we update the sample. Our goal is to provide all of the information needed to underpin theoretical modeling. For each of the two redshifts, $z = 5.7$ and $z = 6.6$, we will release a binary FITS file containing the quantities given in Table 3. Table 3 gives the first release as part of the present paper.

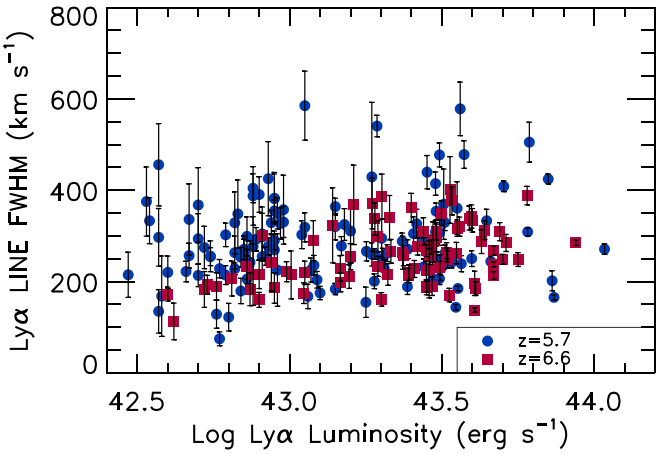

Figure 8. Lyα line width vs. L(Lyα) for our $z = 5.7$ (blue circles) and $z = 6.6$ (red squares) LAEs. The lower-luminosity LAEs show a strong evolution of decreasing line width with increasing redshift, while the high-luminosity LAEs do not. The transition luminosity lies at log L(Lyα) ≈ 43.25 erg s^{-1}. The errors are 68% confidence on the FWHM.

5. Evolution of the Lyα Line Widths with Redshift

In Figure 8, we show our Lyα line widths versus L(Lyα) (blue circles: $z = 5.7$; red squares: $z = 6.6$). As we discuss below, the $z = 5.7$ sample FWHM distribution is relatively uniform over the observed luminosity range. In contrast, the $z = 6.6$ sample FWHM distribution is much narrower at lower luminosities (log L(Lyα) <43.25 erg s^{-1}) than at high luminosities. At high luminosities, the two redshift samples have similar FWHM distributions.

In Figure 9, we compare the FWHM distributions of the full samples (black lines) with those at lower luminosities (shaded regions). At $z = 5.7$, the two distributions are similar, and a Kolmogorov–Smirnov test gives a 0.84 probability that they could be consistent. At $z = 6.6$, the two distributions are quite different, with the lower-luminosity LAEs being narrower. A Kolmogorov–Smirnov test gives only a 4.7×10^{-5} probability that they could be drawn from the same distribution. The high-luminosity LAEs at $z = 6.6$ are consistent with both the high- and low-luminosity LAEs at $z = 5.7$. Comparing the high-luminosity LAEs at the two redshifts gives a Kolmogorov–Smirnov probability of 0.51 (See also the stacked spectra of Figure 2).

These results suggest that, at $z = 6.6$, the high-luminosity LAEs may preferentially lie in more highly ionized regions than the lower-luminosity LAEs, while by $z = 5.7$, the IGM is much more uniformly ionized. We return to this point in the discussion (Section 6).

Our Lyα line widths versus L(Lyα) are mostly consistent with previously published values. In Figure 10, we compare our measurements with the measurements from Shibuya et al. (2018; green circles). We also compare with Ouchi et al. (2010) for fainter LAEs at $z = 6.6$ and with Mallery et al. (2012) for LAEs at $z = 5.7$. We do not compare with Ouchi et al. (2010) for LAEs at $z = 5.7$, as their errors are too large to be useful. We note that, while their $z = 6.7$ errors are also large, within these errors, their data are consistent with the present results. Finally, we compare with the stacked values of Ning et al. (2022; red diamonds), which are in very good agreement with our measurements at $z = 6.6$ but appear to be low at $z = 5.7$.

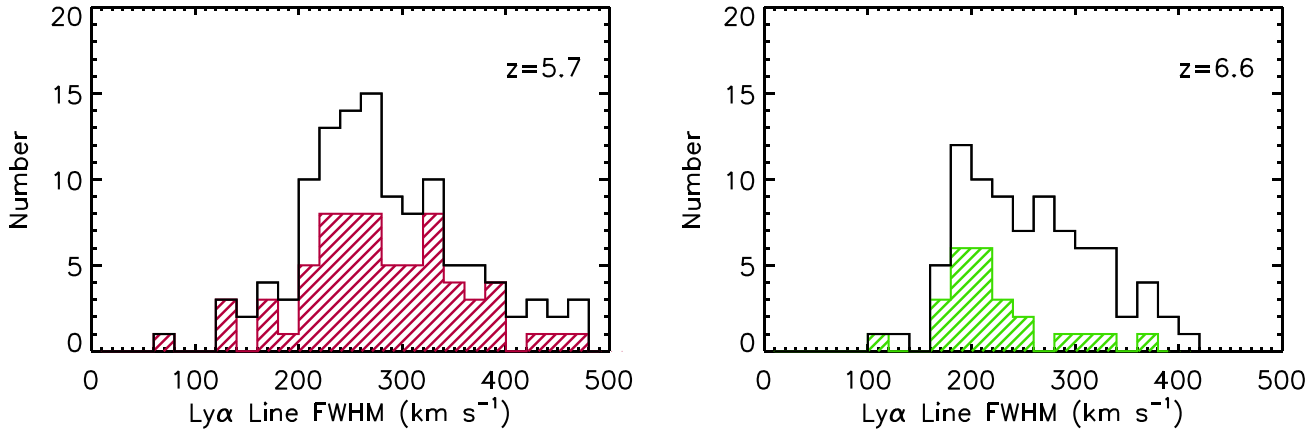

Figure 9. Lyα line FWHM distributions for (left) the $z = 5.7$ LAEs, where the red shading shows the lower-luminosity sources (log L(Lyα) < 43.25 erg s^{-1}), and (right) the $z = 6.6$ LAEs, where the green shading shows the lower-luminosity sources.

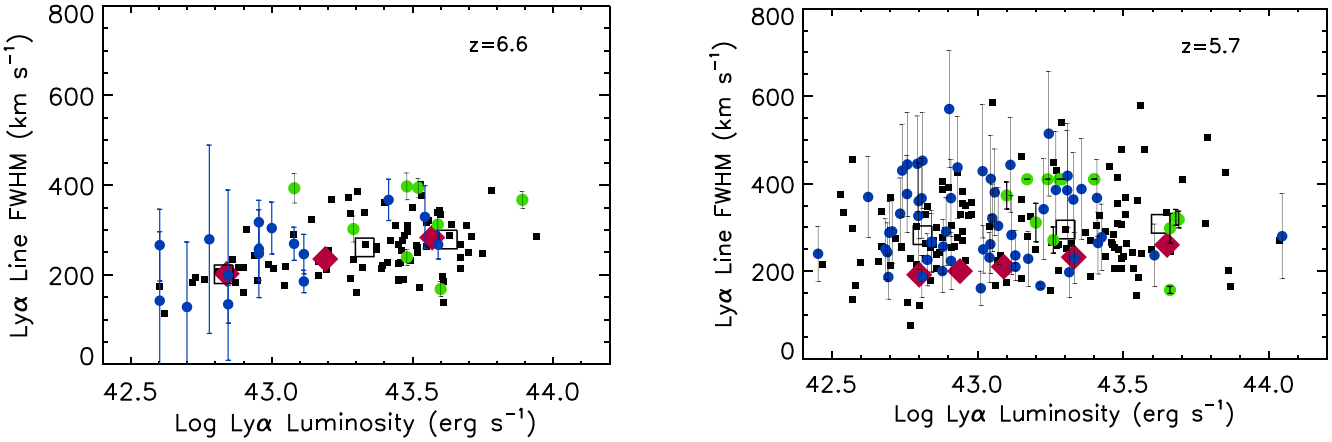

Figure 10. Comparison of our (left) $z = 6.6$ and (right) $z = 5.7$ Lyα line widths (small black squares) and their means (large open squares) with archival data (left: green circles—Shibuya et al. 2018; blue circles—Ouchi et al. 2010; right: green circles—Shibuya et al. 2018; blue circles—Mallery et al. 2012). In both panels, we also show the stacked measurements from Ning et al. (2022; red diamonds). For clarity, we do not show the errors on the present data here, but they are shown in Figure 8. The errors shown on the archival data are the 68% confidence range of the FWHM.

6. Discussion

6.1. Velocity Widths

The differential evolution of the velocity widths with redshift discussed in Section 2 and shown in Figures 8 and 9 implies that the $z = 5.7$ LAEs must lie in a relatively uniformly ionized background, regardless of L(Lyα), while at $z = 6.6$, the high-luminosity LAEs continue to lie in ionized regions, but the lower-luminosity sources show the effects of increasing IGM neutrality. Thus, at $z = 6.6$, it appears that the high-luminosity LAEs either are producing large ionized bubbles themselves, or they are marking overdense galaxy sites that are producing such bubbles, while the lower-luminosity LAEs are not. In order to avoid suppressing the red wings of the LAEs with the radiation-damping wings from surrounding neutral hydrogen in the IGM, we require a surrounding highly ionized region with a size R greater than about 1 pMpc (e.g., Mason & Gronke 2020 and references therein). This size does not depend on the LAE properties but only on the IGM neutrality.

The requirement that the observed LAEs lie in ionized bubbles has been used to estimate lower limits on the fractional ionized volume in the IGM (Malhotra & Rhoads 2006). Here, we use the present data to refine this calculation at $z = 6.6$.

We adopt the radius versus luminosity shape dependence from Yajima et al. (2018), whose normalization agrees closely with the present work. We then take the present results as an empirical normalization of the R–L(Lyα) relation. Using only the shape of the Yajima curve and normalizing to 1 pMpc at our transition log L(Lyα) = 43.25 erg s^{-1}, we obtain

$$R(\text{in pMpc}) = 0.82\ L_{43}^{0.285}, \quad (3)$$

where L_{43} is L(Lyα) in units of 10^{43} erg s^{-1}. Lyα sources fainter then log L(Lyα) = 43.25 erg s^{-1} have bubble sizes smaller than 1 pMpc and will suffer scattering in the red wing.

We can now use this calibration of R to estimate the fractional ionized volume marked by the luminous LAEs. The dependence of the ionized volume around a given LAE is $\propto L(\text{Ly}\alpha)^{0.855}$, so the ionized fraction is dominated by the more numerous lower-luminosity sources. In HEROES, there are 21 sources with log L(Lyα) above 43.5 erg s^{-1}, where the sample is substantially complete (Taylor et al. 2021 give 0.6 for the incompleteness at this luminosity). At log L(Lyα) above 43.4 erg s^{-1}, there are 32 sources in the field, as shown in Figure 11. The small covering area of these very luminous sources can be seen in Figure 11. The observed volume is 82,000 pMpc^3, while the summed incompleteness corrected

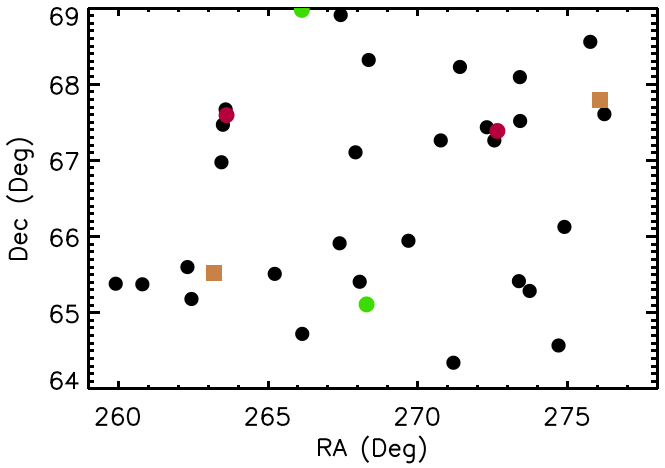

Figure 11. Positions of the 32 $z = 6.6$ LAEs detected in HEROES with log L (Lyα) > 43.4 erg s^{-1}. The two sources with double-peaked Lyα profiles are shown in green, sources with multiple neighbors within 10′ are shown in red, and the two broad-line AGNs are shown as gold squares. The angular sizes of the bubbles are roughly comparable to the sizes of the symbols.

ionized volume for the sources with log L(Lyα) above 43.5 erg s^{-1} is 190 pMpc^3, or 0.2% of the volume at $z = 6.6$.

Because of the shallow dependence of the volume versus luminosity relation of Equation (3), even lower-luminosity sources only mark a small fractional ionized volume. We may generalize and extend to lower luminosities using the Schechter function fit to the $z = 6.6$ LAE LF of Ning et al. (2022; $\alpha = -1.5$, $\log_{10}\phi_\star = -4.26$, and $\log_{10}L_\star = 43.02$, where the units are cMpc^{-3} and erg s^{-1}), we find that ionized regions for LAEs with log L(Lyα) > 42 erg s^{-1} only correspond to about 8% of the volume. This fraction is strictly a lower bound, since it omits yet lower-luminosity LAEs and also ionized regions that do not contain LAEs.

These values are lower than previous estimates made using required ionized bubble sizes at these redshifts. For example, Malhotra & Rhoads (2006) suggested an ionized bubble volume fraction of 20%–50% at $z = 6.5$. The primary difference from their work is the adopted LAE LF. Ning et al. (2022) show a low normalization for the $z = 6.6$ LF, in good agreement with Hu et al. (2010) and up to a factor of 3 lower than some other measurements of the $z = 6.6$ LF. These higher normalizations would raise the fraction closer to the Malhotra & Rhoads (2006) values. However, Ning et al. (2020) attribute such high-normalization LFs to the use of photometric rather than spectroscopic samples, or to field-to-field variation. The dependence on the LF does emphasize the uncertainty of the calculation and that our 8% ionized volume may be a lower limit for this reason also.

6.2. Double-peaked LAEs

Double-peaked LAEs provide an alternative diagnostic of the properties of the highly ionized regions surrounding the LAEs. The conditions for seeing double peaks are more restrictive than for seeing red wings (Mason & Gronke 2020), since the blue side of the HII region also needs to be transmissive, at least to the velocities seen in the blue wing. Mason & Gronke (2020) compute the proximity radius, R_a, where the ionizing flux of the galaxy is sufficient to make the surroundings have a low enough neutral fraction to pass the blue light. This radius then determines the most negative blue velocity that can be seen. Their work indicates that R_a is generally several times smaller than the radius of the ionized bubble.

At $z \sim 3$, ∼30% of LAEs are double-peaked (Kulas et al. 2012). At very low redshifts, a large fraction of Green Pea samples (e.g., Henry et al. 2015; Yang et al. 2017) show blue-side emission, with ∼30% showing strong blue-side peaks (i.e., the blue peak value exceeds 25% of the red peak value).

Here, we quantify the double-peaked fractions at $z = 5.7$ and $z = 6.6$ to compare with each other and with the low-redshift fraction. We restrict to high-quality spectra, where the signal-to-noise ratio (S/N) of the amplitude in the spectral fits exceeds 7. To make an objective selection, we take the redshift of the main peak and blank the 2D spectral image redward of −120 km s^{-1}. This choice minimizes contamination from the blue tail of the main peak, given the resolution of the spectroscopic observations. We then search the central region of the blanked 2D image (±0.″6 from the slit position of the main peak) for secondary peaks, requiring that the S/N in the secondary peak lies above 4σ and that the secondary peak value exceeds 25% of the main peak value. Finally, we restrict to secondary peaks with velocities redward of −800 km s^{-1} relative to the main peak velocity. Our final sample therefore corresponds to source with double peak separations between 120 and 800 km s^{-1}. After visual inspection, we decided that apparent double peaks in two of the $z = 5.7$ LAEs were artifacts; thus, hereafter, we consider them as single-peaked LAEs.

At $z = 6.6$, four of the 71 high-quality LAEs that we searched are double-peaked sources. We show these in Figure 12 (two of the four are our previously published sources COLA1 and NEPLA4, while the other two are more marginal detections). At $z = 5.7$, 15 of the 107 high-quality LAEs that we searched are double-peaked sources. We show four examples in Figure 13. We mark the double-peaked sources using flag = 2 in Table 3.

In Figure 14, we plot the peak separations of our double-peaked LAEs versus log L(Lyα). We also show the low-redshift Green Pea galaxy sample of Yang et al. (2017) and the $z = 6.9$ double-peaked LAE of Meyer et al. (2021), where this information is available. We do not have such quantitative information for the intermediate-redshift samples.

At $z = 5.7$, the fraction of double-peaked LAEs at log L (Lyα) > 43.25 erg s^{-1} is consistent with the overall fraction at this redshift (14% ± 4%). At $z = 6.6$, the fraction of double-peaked LAEs is 6(3–10)%. We do not see any double peaks in lower-luminosity sources at $z = 6.6$, though we note that the $z = 6.9$ double-peaked LAE of Meyer et al. (2021) lies at lower luminosity. At both redshifts, the fraction of double-peaked LAEs is low compared to the 30% seen at $z \lesssim 3$. This is consistent with our expectation that the blue-side scattering by neutral material in the ionized regions may be obscuring the blue peaks in a significant fraction of the sources at these redshifts, despite their having substantially unobscured red-side emission.

The proximity radius is larger for sources with brighter near-UV (NUV) luminosities, so we might expect the double-peaked LAEs preferentially to have higher 1500 Å absolute magnitudes (M1500). Indeed, all of the double-peaked LAEs have detected Y magnitudes, which we have used to compute M1500 following Matthee et al. (2018), though NEPLA4 is only detected at the 2σ level. We do not attempt to correct for the contributions of the Lyα line in the wing of the Y band, which

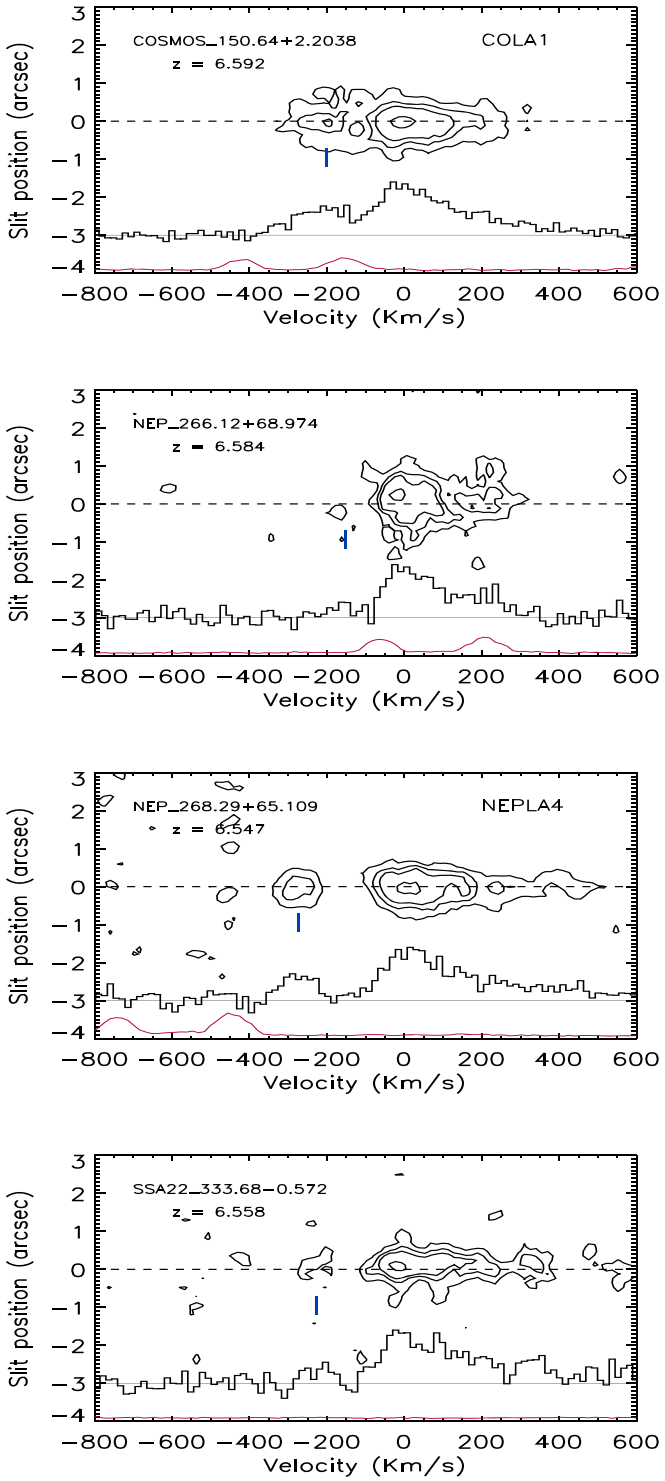

Figure 12. Two-dimensional spectral images of the four double-peaked sources in the $z = 6.6$ sample. The contour levels are 0.2, 0.36, 0.5, and 0.9 times the red peak value. We previously published two of these (COLA1 and NEPLA4), which we label. The dashed line marks the slit center, and the small blue vertical line the second peak. The 1D spectrum is also shown, together with the sky spectrum (red), both of which have arbitrary normalizations to fit on the plot.

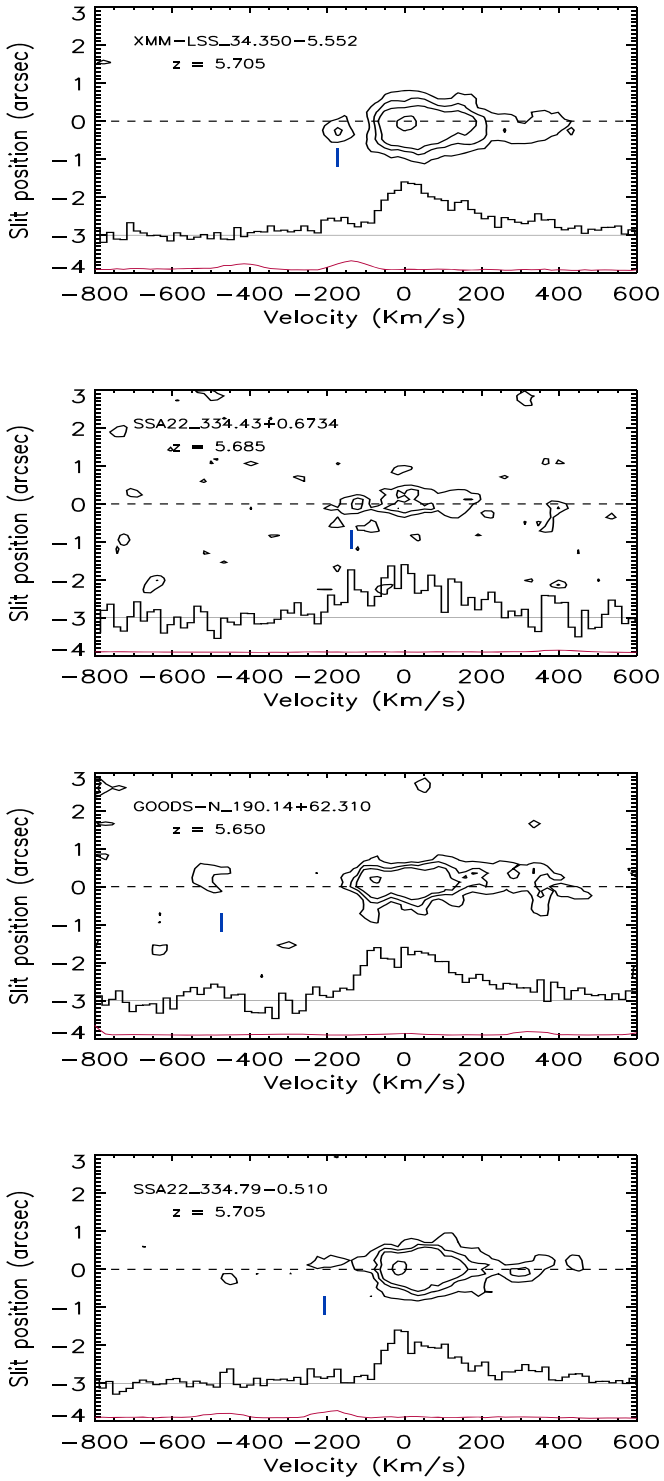

Figure 13. Two-dimensional spectral images of four of the 15 double-peaked sources in the $z = 5.7$ sample. The contour levels are 0.2, 0.36, 0.5, and 0.9 times the red peak value. The dashed line marks the slit center, and the small blue vertical line the second peak. The 1D spectrum is also shown, together with the sky spectrum (red), both of which have arbitrary normalizations to fit on the plot.

would only make the M1500 fainter. (The error bars for all the sources are shown in Figure 15.) In Figure 15, we compare the double-peaked LAEs with other LAEs in the HEROES and SSA22 fields. We can see that the double-peaked LAEs (larger symbols) are among the brighter NUV sources, with M1500 magnitudes in the range from −21 to −22.5.

Mason & Gronke (2020) computed models for the proximity radius at $z = 6.6$ and the corresponding peak velocity

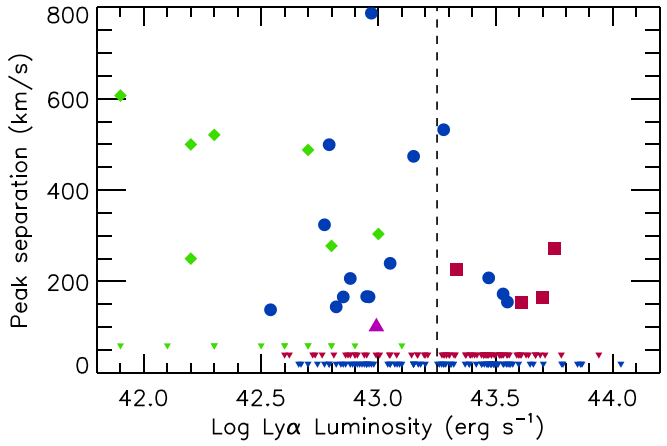

Figure 14. Peak velocity separation vs. log L(Lyα) for the $z = 6.6$ double-peaked LAEs (red squares) and the $z = 5.7$ double-peaked LAEs (blue circles). We also show the double-peaked sources in the low-redshift Green Pea galaxy sample of Yang et al. (2017; green diamonds) and the $z = 6.9$ double-peaked LAE of Meyer et al. (2021; purple triangle). Sources without double peaks are marked with small triangles at the bottom of the figure (red is $z = 6.6$, blue is $z = 5.7$). The Green Pea sources that do not satisfy our double peak definition are shown as green triangles.

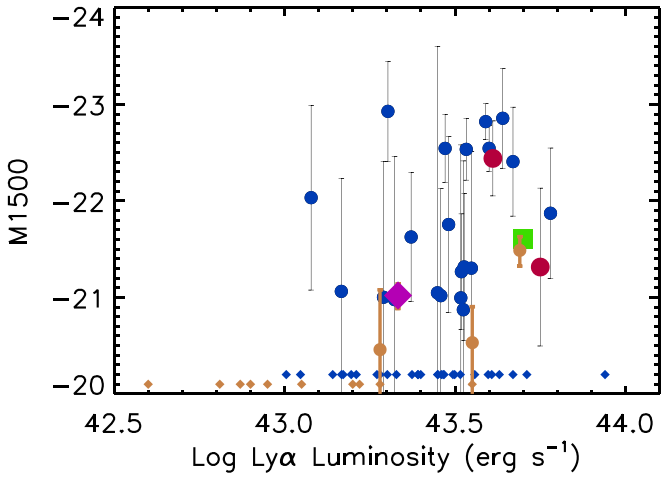

Figure 15. UV absolute magnitude at 1500 Å vs. log L(Lyα) for the $z = 6.6$ LAEs in HEROES (blue circles) and SSA22 (gold circles). The Y magnitudes used to calculate M1500 in HEROES are the Kron magnitudes from Taylor et al. (2023). Detected sources are shown with 1σ error bars. Undetected sources are shown as small diamonds at nominal values of −21.8 (HEROES) and −21.9 (SSA22). The two double-peaked LAEs in HEROES are shown as red circles, and the one in SSA22 as a purple diamond. COLA1 (green square) is shown using the M1500 value from Matthee et al. (2018).

separation as a function of the NUV luminosity. In Figure 16, we show that three of our four $z = 6.6$ double-peaked LAEs lie beneath the Mason & Gronke (2020) reference model (black curve) for the peak velocity separation and are therefore inconsistent with this model (as Mason & Gronke 2020 pointed out for COLA1). However, the Mason & Gronke (2020) models show that reducing the local gas density by a factor of 2 (green curve) would permit the transmission of the blue peaks.

As Mason & Gronke (2020) point out, their reference model is highly optimistic, assuming an escape fraction of one and no clumping, so even the green curve may not be sufficient. For example, Meyer et al. (2021) argue via comparison of the peak velocity separations of such wide sources with those of local peak separations that the escape fractions should be considerably lower, with values of around 0.1–0.2 (Izotov et al. 2018).

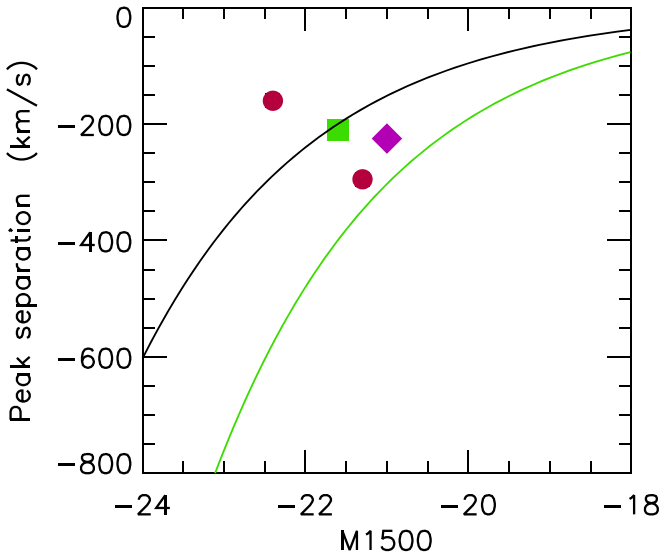

Figure 16. Peak velocity separation vs. UV absolute magnitude at 1500 Å for the $z = 6.6$ double-peaked LAEs (red circles—HEROES; green square—COLA1; purple diamond—SSA22-333.68-0.572). The black curve shows the reference model of Mason & Gronke (2020), while the green curve shows the same model but with half the average density in the neighborhood of the source.

Thus, multiple ionizing sources in the vicinity of the double-peaked LAEs may be required in order to generate the large proximity radii necessary to see the blue peaks in these sources. Deeper observations in both the continuum and Lyα in the vicinity of the double-peaked LAEs are clearly needed in order to examine this possibility.

7. Summary

We present two uniformly observed large spectroscopic samples of LAEs (127 at $z = 5.7$ and 82 at $z = 6.6$) from our Keck/DEIMOS follow-up of narrowband-selected sources in the large, contiguous HEROES field (44 deg^2), plus several smaller fields from the Subaru/HSC and Subaru/Suprime-Cam archives. Our main results are as follows.

The generic spectral shape of the average Lyα line profile at these redshifts, with a sharp break at the blue side and a tail to the red side, belies the diversity of individual line shapes and widths that we see. This emphasizes the need for large spectroscopic samples, such as the present atlas, which can be combined with models of the IGM density and ionization structure to predict the LAE properties at higher redshifts.

Large spectroscopic samples, such as the present atlas, also reveal rare and interesting objects. We found small numbers of LAEs with double-peaked Lyα profiles; very extended red wings; broad-line AGNs; and a unique lensed LAE cross.

By comparing the Lyα line widths for the LAEs at the two redshifts, we found that the FWHM distribution for the $z = 5.7$ sample is relatively uniform over the observed luminosity range, while that for the $z = 6.6$ sample is not: it is much narrower at lower luminosities (log L(Lyα) <43.25 erg s^{-1}) than at high luminosities. The $z = 5.7$ and $z = 6.6$ samples have similar FWHM distributions at high luminosities. This suggests that, at $z = 6.6$, the high-luminosity LAEs may preferentially lie in more highly ionized regions than the lower-luminosity LAEs. The ionized regions constitute at least 8% of the volume at $z = 6.6$, but this estimate is quite uncertain and depends strongly on the adopted Lyα LF.

At $z = 5.7$, about 14% of the LAEs have double peaks, while at $z = 6.6$, this has dropped to about 6%. This can be compared with the 30% seen at lower redshifts. Comparing the observed $z = 6.6$ double peaks with the models of Mason & Gronke (2020) suggests that the LAEs themselves are not UV luminous enough to ionize the surrounding regions to the required level (see also Meyer et al. 2021). The double-peaked Lyα profiles may therefore mark sites with multiple ionizing sources.

In future work, we plan to migrate our ongoing spectroscopic follow-up from Keck/DEIMOS to the Keck/KCWI integral field spectrograph, which will provide spatially resolved spectra of the LAEs and also allow us to search for neighboring ionizing sources.

Acknowledgments

We gratefully acknowledge support for this research from NSF grants AST-1716093 (A.S., E.M.H.) and AST-1715145 (A.J.B), NASA grant 80NSSC24K0618, a Kellett Mid-Career Award, and a WARF Named Professorship from the University of Wisconsin-Madison Office of the Vice Chancellor for Research and Graduate Education with funding from the Wisconsin Alumni Research Foundation (A.J.B.) and the William F. Vilas Estate (A.J.T.).

The Hyper Suprime-Cam (HSC) collaboration includes the astronomical communities of Japan and Taiwan, and Princeton University. The HSC instrumentation and software were developed by the National Astronomical Observatory of Japan (NAOJ), the Kavli Institute for the Physics and Mathematics of the Universe (Kavli IPMU), the University of Tokyo, the High Energy Accelerator Research Organization (KEK), the Academia Sinica Institute for Astronomy and Astrophysics in Taiwan (ASIAA), and Princeton University. Funding was contributed by the FIRST program from the Japanese Cabinet Office, the Ministry of Education, Culture, Sports, Science and Technology (MEXT), the Japan Society for the Promotion of Science (JSPS), Japan Science and Technology Agency (JST), the Toray Science Foundation, NAOJ, Kavli IPMU, KEK, ASIAA, and Princeton University.

This paper is based on data collected at the Subaru Telescope and retrieved from the HSC data archive system, which is operated by the Subaru Telescope and Astronomy Data Center (ADC) at NAOJ. Data analysis was in part carried out with the cooperation of Center for Computational Astrophysics (CfCA), NAOJ.

This paper makes use of software developed for the Vera C. Rubin Observatory. We thank the Rubin Observatory for making their code available as free software.

We wish to recognize and acknowledge the very significant cultural role and reverence that the summit of Maunakea has always had within the indigenous Hawaiian community. We are most fortunate to have the opportunity to conduct observations from this mountain.

Facilities: Keck:II, Subaru

ORCID iDs

A. Songaila https://orcid.org/0000-0001-9028-6978
L. L. Cowie https://orcid.org/0000-0002-6319-1575
A. J. Barger https://orcid.org/0000-0002-3306-1606
E. M. Hu https://orcid.org/0009-0008-7427-4617
A. J. Taylor https://orcid.org/0000-0003-1282-7454

References

Aihara, H., AlSayyad, Y., Ando, M., et al. 2022, PASJ, 74, 247
Becker, G. D., Bolton, J. S., Madau, P., et al. 2015, MNRAS, 447, 3402
Bosman, S. E. I., Kakiichi, K., Meyer, R. A., et al. 2020, ApJ, 896, 49
Bunker, A. J., Saxena, A., Cameron, A. J., et al. 2023, A&A, 677, A88
Claeyssens, A., Richard, J., Blaizot, J., et al. 2019, MNRAS, 489, 5022
Cowie, L. L., Songaila, A., Hu, E. M., & Cohen, J. G. 1996, AJ, 112, 839
Fuller, S., Lemaux, B. C., Bradač, M., et al. 2020, ApJ, 896, 156
Garaldi, E., Kannan, R., Smith, A., et al. 2022, MNRAS, 512, 4909
Garel, T., Blaizot, J., Guiderdoni, B., et al. 2015, MNRAS, 450, 1279
Garel, T., Blaizot, J., Rosdahl, J., et al. 2021, MNRAS, 504, 1902
Goto, H., Shimasaku, K., Yamanaka, S., et al. 2021, ApJ, 923, 229
Greene, J. E., Labbe, I., Goulding, A. D., et al. 2024, ApJ, 964, 39
Guo, Y., Bacon, R., Wisotzki, L., et al. 2023, arXiv:2309.06311
Haiman, Z. 2002, ApJL, 576, L1
Haiman, Z., & Cen, R. 2005, ApJ, 623, 627
Harikane, Y., Zhang, Y., Nakajima, K., et al. 2023, ApJ, 959, 39
Hashimoto, T., Laporte, N., Mawatari, K., et al. 2018, Natur, 557, 392
Hassan, S., & Gronke, M. 2021, ApJ, 908, 219
Henry, A., Scarlata, C., Martin, C. L., & Erb, D. 2015, ApJ, 809, 19
Hoag, A., Bradač, M., Brammer, G., et al. 2018, ApJ, 854, 39
Hoag, A., Bradač, M., Huang, K., et al. 2019, ApJ, 878, 12
Hu, E. M., Cowie, L. L., Barger, A. J., et al. 2010, ApJ, 725, 394
Hu, E. M., Cowie, L. L., Songaila, A., et al. 2016, ApJL, 825, L7
Itoh, R., Ouchi, M., Zhang, H., et al. 2018, ApJ, 867, 46
Izotov, Y. I., Worseck, G., Schaerer, D., et al. 2018, MNRAS, 478, 4851
Jansen, R. A., & Windhorst, R. A. 2018, PASP, 130, 124001
Jensen, H., Laursen, P., Mellema, G., et al. 2013, MNRAS, 428, 1366
Jiang, L., Shen, Y., Bian, F., et al. 2017, ApJ, 846, 134
Katz, H., Rosdahl, J., Kimm, T., et al. 2023, OJAp, 6, 44
Kikuta, S., Ouchi, M., Shibuya, T., et al. 2023, ApJS, 268, 24
Kocevski, D. D., Onoue, M., Inayoshi, K., et al. 2023, ApJL, 954, L4
Konno, A., Ouchi, M., Ono, Y., et al. 2014, ApJ, 797, 16
Konno, A., Ouchi, M., Shibuya, T., et al. 2018, PASJ, 70S, 16
Kulas, K. R., Shapley, A. E., Kollmeier, J. A., et al. 2012, ApJ, 745, 33
Kusakabe, H., Blaizot, J., Garel, T., et al. 2020, A&A, 638, A12
Larson, R. L., Finkelstein, S. L., Hutchison, T. A., et al. 2022, ApJ, 930, 104
Laursen, P., Sommer-Larsen, J., & Razoumov, A. O. 2011, ApJ, 728, 52
Malhotra, S., & Rhoads, J. E. 2006, ApJL, 647, L95
Mallery, R. P., Mobasher, B., Capak, P., et al. 2012, ApJ, 760, 128
Mason, C. A., & Gronke, M. 2020, MNRAS, 499, 1395
Matthee, J., Sobral, D., Darvish, B., et al. 2017, MNRAS, 472, 772
Matthee, J., Sobral, D., Gronke, M., et al. 2018, A&A, 619, A136
Meyer, R. A., Laporte, N., Ellis, R. S., Verhamme, A., & Garel, T. 2021, MNRAS, 500, 558
Neyer, M., Smith, A., Kannan, R., et al. 2024, MNRAS, 531, 2943
Ning, Y., Jiang, L., Zheng, Z.-Y., et al. 2020, ApJ, 903, 4
Ning, Y., Jiang, L., Zheng, Z.-Y., & Wu, J. 2022, ApJ, 926, 230
Oesch, P. A., van Dokkum, P. G., Illingworth, G. D., et al. 2015, ApJL, 804, L30
Ouchi, M., Shimasaku, K., Furusawa, H., et al. 2010, ApJ, 723, 869
Pentericci, L., Vanzella, E., Castellano, M., et al. 2018, A&A, 619, A147
Santos, S., Sobral, D., & Matthee, J. 2016, MNRAS, 463, 1678
Shibuya, T., Ouchi, M., Harikane, Y., et al. 2018, PASJ, 70S, 15
Shibuya, T., Ouchi, M., Nakajima, K., et al. 2014, ApJ, 785, 64
Sobral, D., Matthee, J., Darvish, B., et al. 2015, ApJ, 808, 139
Songaila, A., Barger, A. J., Cowie, L. L., Hu, E. M., & Taylor, A. J. 2022, ApJ, 935, 52
Songaila, A., Hu, E. M., Barger, A. J., et al. 2018, ApJ, 859, 91
Stark, D. P. 2016, ARA&A, 54, 761
Stark, D. P., Ellis, R. S., Chiu, K., Ouchi, M., & Bunker, A. 2010, MNRAS, 408, 1628
Taylor, A. J., Barger, A. J., Cowie, L. L., et al. 2023, ApJS, 266, 24
Taylor, A. J., Barger, A. J., Cowie, L. L., Hu, E. M., & Songaila, A. 2020, ApJ, 895, 132
Taylor, A. J., Cowie, L. L., Barger, A. J., Hu, E. M., & Songaila, A. 2021, ApJ, 914, 79
Wold, I. G. B., Malhotra, S., Rhoads, J., et al. 2022, ApJ, 927, 36
Xu, C., Smith, A., Borrow, J., et al. 2023, MNRAS, 521, 4356
Yajima, H., Sugimura, K., & Hasegawa, K. 2018, MNRAS, 477, 5406
Yang, H., Malhotra, S., Gronke, M., et al. 2017, ApJ, 844, 171
Yang, H., Wang, J., Zheng, Z.-Y., et al. 2014, ApJ, 784, 35
Zitrin, A., Labbé, I., Belli, S., et al. 2015, ApJL, 810, L12